Sphingomyelin biosynthesis is essential for phagocytic signaling during *Mycobacterium tuberculosis* host cell entry

Patrick Niekamp†[1,2], Gaelen Guzman†[1], Hans Leier[1], Ali Rashidfarrokhi[3], Veronica Richina[4], Fabian Pott[1], Joost C. M. Holthuis[2], Fikadu G. Tafesse[1]‡

†These authors contributed equally.

[1]Department of Molecular Microbiology and Immunology, Oregon Health & Science University, 3181 SW Sam Jackson Park Road, Portland, OR 97239. [2]Biology & Chemistry Department, University of Osnabrück, Fachbereich Biologie/Chemie, Barbarastrasse 13, 49076 Osnabrück, Germany. [3]Department of Pathology and Department of Medicine, New York University Langone, 550 First Avenue, MSB 594, New York, NY 10016. [4]Department of Biomedicine University Basel Hebelstrasse 20, 4031 Basel, Switzerland.

‡Correspondence: Fikadu G. Tafesse, Department of Molecular Microbiology and Immunology, Oregon Health & Science University, 3181 SW Sam Jackson Park Road, Portland, OR 97239.
Email: tafesse@ohsu.edu

18 **Abstract**

19 *Mycobacterium tuberculosis* (Mtb) invades alveolar macrophages through phagocytosis to
20 establish infection and cause disease. The molecular mechanisms underlying Mtb entry are still
21 poorly understood. Here, we report that an intact sphingolipid biosynthetic pathway is essential
22 for the uptake of Mtb across multiple phagocytic cell types without affecting other forms of
23 endocytosis. Disrupting sphingolipid production prevents the removal of the inhibitory
24 phosphatase CD45 from the nascent phagosome, a critical step in the progression of phagocytosis.
25 We also show that blocking sphingolipid biosynthesis impairs activation of Rho GTPases, actin
26 dynamics and phosphoinositide turnover at the host-pathogen contact site. Moreover, production
27 of sphingomyelin, not glycosphingolipids, is critical for the uptake of Mtb. Together, our data
28 provide mechanistic insights regarding how Mtb exploits sphingomyelin metabolism to enter host
29 cells, representing a potential avenue for designing host-directed therapeutics against tuberculosis.

30 **Introduction**

31

32 *Mycobacterium tuberculosis* (Mtb), the etiologic agent of tuberculosis, remains a significant global
33 health threat. It is estimated that more than two billion people around the world are infected with
34 the latent form of Mtb and about 1.5 million die every year (*1*). The success of Mtb as a pathogen
35 relies on its ability to effectively enter the immune cells and establish its niche by subverting the
36 defense mechanisms of the host (*2*, *3*). Elucidating these mechanisms will help us to understand
37 the complex host-pathogen interfaces and design a therapeutic strategy to combat this disease.

38

39 Phagocytosis of Mtb by lung resident alveolar macrophages represents the obligate first step in the
40 Mtb infection cycle. Phagocytic cells of the immune system consist predominantly of
41 macrophages, dendritic cells and neutrophils and are responsible for the production of key effector
42 molecules critical for instigating the adaptive immune responses (*4*). Phagocytosis is a complex
43 cellular process that begins with the binding of pathogens to the cell surface through the interaction
44 of pattern recognition receptors (PRRs) with ligands on the surface of the pathogen (*5*, *6*). During
45 this process, phagocytes undergo extensive membrane reorganization and cytoskeleton
46 rearrangement at their cell surface to engulf the pathogen. Conceivably, the lipid composition of
47 the plasma membrane plays an essential role in regulating the lateral movement of receptors and
48 signaling molecules to form the phagocytic synapse (*6*, *7*). While a great deal of effort has been
49 devoted to understanding the proteins and signaling molecules such as phosphoinositides in this
50 process, the contribution of other membrane lipids such as sphingolipids in Mtb phagocytosis
51 remains unknown.

52

53 Sphingolipids are a diverse class of lipids that contain a sphingoid base and are conserved in all
54 eukaryotes. Although their distribution among the various biological organelles is distinct,
55 sphingolipids are mainly enriched at the outer leaflet of the plasma membrane (*8–10*). Therefore,
56 pathogens including Mtb inevitably interact with this class of lipids during phagocytosis. The *de*
57 *novo* biosynthetic pathway of sphingolipids starts with the condensation of serine and palmitoyl
58 CoA to yield 3-ketodihydrosphingosine, in a reaction catalyzed by serine palmitoyl CoA
59 transferase (SPT) (*9*). Subsequent reactions yield ceramide, the backbone of all sphingolipids,
60 which is then delivered to the Golgi apparatus to be converted to sphingomyelin or
61 glycosphingolipids (Figure 1A) (*9*, *10*). These molecules are known mediators of a diverse array
62 of cellular functions and signaling, have critical roles in membrane organization at the cell surface
63 (*11*, *12*). Moreover, sphingolipids are essential for the transport of viral glycoproteins from the
64 Golgi apparatus to the cell surface and for the trafficking of bacterial toxins across the endocytic
65 pathway (*13*, *14*). Although the type of sphingolipid species and their mechanism of actions
66 remained to be determined, recent studies have shown a role for sphingolipids in *in vivo* clearance
67 of the pathogenic fungi *Candida albicans* through phagocytosis (*15*). Thus far, we know little
68 about whether bioactive and structural sphingolipids play a role in Mtb invasion of phagocytic
69 immune cells.
70
71 Here we show that Mtb requires host sphingolipids to effectively invade both macrophages and
72 dendritic cells. Perturbation of sphingolipid biosynthesis through CRISPR/Cas9 gene editing, or
73 small molecule inhibitors that target the key enzymes in the sphingolipid biosynthetic pathway,
74 remarkably reduces Mtb uptake in different phagocytic cell types without affecting other forms of
75 receptor-mediated endocytosis. Employing extensive time-lapse live imaging, we determined that

76 sphingolipids are critical in the removal of the inhibitory phosphatase CD45 from the receptor-
77 pathogen contact sites, an essential step in the progression of a phagocytic synapse. We also found
78 that macrophages deficient in sphingolipid biosynthesis are defective in phosphoinositide
79 turnover, F-actin remodeling and activation of the small GTPases Rac1 and CDC42. We further
80 determined that biosynthesis of sphingomyelin, not glycosphingolipids, is critical for the
81 phagocytosis of Mtb by macrophages. These data demonstrate a role for sphingomyelin
82 biosynthesis in an early step of Mtb infection, defining a potential target for host-directed anti-
83 mycobacterial therapeutics.
84

85 **Results**

86 **Manipulation of sphingolipid levels in mammalian phagocytes using pharmacological and**
87 **genetic tools**

88 To define the role of the sphingolipid biosynthetic pathway in phagocytic uptake of Mtb, we sought
89 to inhibit sphingolipid biosynthesis in four different phagocytic cell lines: the murine macrophage
90 cell line RAW 246.7, the murine dendritic cell line DC2.4, and the human monocyte cell lines
91 THP-1 and U937 (Figure 1B). As depicted in Figure 1A, the initial and rate limiting step of
92 sphingolipid synthesis is the production of the sphingoid base through the condensation of serine
93 and palmitoyl-CoA, a reaction performed by the serine palmitoyltransferase (SPT) enzyme
94 complex (*9*). Previously, we reported that genetic ablation of the SPT subunit Sptlc2 blocks the *de*
95 *novo* synthesis of all sphingolipids, as does treatment with the atypical amino acid myriocin (Myr)
96 (*15*). The fungal toxin fumonisin B1 (FB1) acts several steps downstream in the sphingolipid
97 biosynthetic pathway by blocking the activity of ceramide synthases (*15*). As the central nexus of
98 sphingolipid biosynthesis, ceramide is converted into a variety of complex sphingolipids,
99 including sphingomyelin and glycosphingolipids (*9*, *16*).

100

101 To verify the reported effects of Myr and FB1 on *de novo* sphingolipid biosynthesis, we monitored
102 the incorporation of 3-L-[^{14}C]-serine into sphingolipid species in RAW 246.7, THP-1, DC2.4 and
103 U937 cells after 3 days of drug treatment using thin layer chromatography analysis. Across all four
104 cell lines examined, treatment with Myr or FB1 in each case reduced incorporation of the serine
105 isotope into sphingomyelin by more than 90%; in contrast, incorporation of the isotope into
106 phosphatidylserine was largely unaffected (Figure 1D, 1E and 1F; Supplemental Figure 1). Genetic

107 ablation of Sptlc2 in RAW 246.7 and DC2.4 cells gave the same results (Figure 1C, 1D and 1E;
108 Supplemental Figure 1), in line with our previous findings (*15*).
109
110 We next examined the impact of drug treatment and Sptlc2 removal on the steady state
111 sphingolipid levels. Both Myr-treated and Sptlc2$^{-/-}$ cells contained significantly reduced levels of
112 sphingosine, ceramides, sphingomyelin and glucosylceramide in comparison to control cells
113 (Figure 1 G-J). In FB1-treated cells, we observed a reduction in the levels of ceramide,
114 sphingomyelin and glucosylceramide concomitant with an increase in sphingosine levels, as
115 expected (Figure 1G-J) (*17*). The residual sphingolipid levels detected in Sptlc2$^{-/-}$, Myr- and FB1-
116 treated cells are likely due to the activity of sphingolipid salvage pathways, through which cells
117 may acquire sphingolipids from additives in the culture medium – primarily serum. This enables
118 them to bypass the growth defect that is generally observed when sphingolipid biosynthetic
119 mutants are cultured in serum-depleted medium. Indeed, we observed that Sptlc2$^{-/-}$ DC2.4 and
120 Sptlc2$^{-/-}$ RAW 264.7 cells grew equally well in serum-containing medium as their wild type
121 counterparts (Supplementary Figure 2) (*15*).
122
123 **Cells deficient in sphingolipid biosynthesis display a reduced capacity to phagocytose Mtb**
124 To address whether sphingolipids participate in the phagocytic uptake of Mtb, RAW 264.7, THP-
125 1, DC2.4, and U937 cells were treated with Myr and FB1 for 3 days and then infected with a
126 mCherry-expressing strain of Mtb (Figure 2A). In brief, cells were infected at a multiplicity of
127 infection (MOI) of 10 for 2 h, fixed and then stained with DyLight 488-conjugated phalloidin and
128 DAPI to visualize F-actin and cell nuclei, respectively. Fluorescence microscopy was used to
129 quantify uptake efficiency by automated counting of cell number (by nuclei) and internalized

130 bacteria (red fluorescent particles within green cell boundary). Uptake efficiency is defined as the
131 ratio of the total number of internalized Mtb particles against the total number of identified nuclei.
132 The ratio is reported as a percentage of phagocytosis relative to the control cells. In all four cell
133 models analyzed, we observe that Myr and FB1 treatment caused a significant (40-60%) reduction
134 in Mtb uptake (Figure 2B-I). Similarly, the knockout of Sptlc2 in RAW 264.7 and DC2.4 cells
135 results in a ~50% reduction in uptake relative to their wild type controls (Figure 3A-D).
136 Collectively, these results indicate that an intact sphingolipid biosynthetic pathway is essential for
137 an efficient uptake of Mtb by professional phagocytes.
138

139 **Sptlc2$^{-/-}$ cells are permissive to endocytic uptake of Herpes Simplex Virus (HSV)**

140 To determine whether an intact sphingolipid biosynthetic pathway is a general prerequisite for the
141 entry of pathogens in professional phagocytes, we performed parallel infections of Sptlc2$^{-/-}$ and
142 wild type RAW 264.7 cells with a fluorescent reporter strain of Herpes Simplex Virus-1 (HSV-1)
143 encoding a fusion of the viral protein VP26 and mCherry (*18*). HSV-1 is an enveloped virus that
144 gains entry to host cells through the phagocytosis-like process of micropinocytosis; the viral
145 receptor involved is nectin-1, also known as herpesviruses entry mediator (*19*). Previous work
146 revealed that HSV-1 entry is dependent on cholesterol (*20*). At 12 h post-infection, we quantified
147 the rates of HSV-1 infection using high-content imaging as described above. Because the VP26-
148 mCherry reporter construct localizes to the nucleus, we did not stain cells using phalloidin and
149 instead used the co-localization of DAPI with mCherry to determine infection efficiency.
150 However, we observe no significant difference in the HSV-1 infection rates between wild type and
151 Sptlc2$^{-/-}$ cells (Figure 3E and 3F). These data indicate that sphingolipid biosynthesis is dispensable

152 for HSV-1 entry and support a more specific role of sphingolipids in the phagocytic uptake of
153 Mtb.
154
155 **Sptlc2$^{-/-}$ cells fail to exclude CD45 from the contact site of pathogen-mimicking particles**
156 We next investigated whether blocking sphingolipid biosynthesis also affects the phagocytic
157 uptake of Zymosan A particles. These pathogen-mimicking particles have been shown to engage
158 the C-type Lectin receptor Dectin-1 on professional phagocytes (*15*, *21*). Dectin-1 is one of several
159 pathogen recognition receptors that engage Mtb and initiate phagocytic signaling to facilitate host
160 cell entry (*22*). Interestingly, Sptlc2$^{-/-}$ RAW 264.7 cells displayed a ~40% reduction in the
161 phagocytic uptake of Zymosan A relative to wild type cells, analogous to Mtb uptake (Figure 3G
162 and 3H). This led us to use Zymosan A as a model particle in subsequent experiments, in which
163 we aimed to define which step in phagocytosis relies on an intact sphingolipid biosynthetic
164 pathway.
165
166 The engagement of pathogen recognition receptors with their ligands initiates receptor clustering
167 at the phagocytic cup, followed by a lateral segregation of the inhibitory phosphatase CD45 (*7*).
168 Because sphingolipids have been implicated as active participants in the organization of signaling
169 complexes at the cell surface (*23*), we reasoned that sphingolipid levels at the plasma membrane
170 may be critical for the aggregation of Dectin-1 and/or exclusion of CD45 from that pathogen
171 contact site. To experimentally address this idea, we transfected wild type and Sptlc2$^{-/-}$ RAW 264.7
172 cells with a GFP-tagged Dectin-1 construct and assessed the co-localization of the fluorescent
173 receptor with CD45 following treatment with non-fluorescent Zymosan A particles. In both wild
174 type and Sptlc2$^{-/-}$ cells, Dectin-1 aggregated at the Zymosan A contact site within two minutes

175 after particle exposure, indicating that sphingolipid biosynthesis is dispensable for ligand-induced
176 receptor clustering. As expected, in wild type cells the inhibitory phosphatase CD45 was
177 efficiently segregated from the Dectin-1 clusters at the particle contact site (Figure 4A upper panels
178 and B) (*7*). In contrast, CD45 failed to segregate from the Dectin-1 clusters in Zymosan A-treated
179 Sptlc2$^{-/-}$ cells (Figure 4A lower panels and B).
180
181 To address whether a block in sphingolipid biosynthesis affects the overall surface expression of
182 CD45 and Dectin-1, wild type and Sptlc2$^{-/-}$ RAW 264.7 cells were stained with APC-conjugated
183 anti-CD45 and FITC-conjugated anti-Dectin-1 antibodies and subjected to analytical flow
184 cytometry. We found no differences in the overall fluorescent signals for both markers between
185 wild type and Sptlc2$^{-/-}$ cells (Figure 4C-F), indicating that the cell surface levels of endogenous
186 Dectin-1 and CD45 are unaffected by blocking sphingolipid biosynthesis. From this we conclude
187 that an intact sphingolipid biosynthetic pathway is required to enable a proper displacement of
188 CD45 from the site of Dectin-1 clustering, a step critical for the initiation of phagocytic synapse
189 formation.
190
191 **Activation of Rho GTPases Rac1 and Cdc42 is impaired in Sptlc2$^{-/-}$ cells**
192 Phagocytosis is strictly regulated through a signaling network that involves the recruitment of
193 pathogen receptors and Rho GTPases to the particle contact site. Activated Rho GTPases promote
194 the conversion of phosphatidylinositol-4-phosphate (PI4P) to phosphatidylinositol-4,5-
195 *bis*phosphate (PIP2) by stimulating phosphatidylinositol 5-kinase (PI5K). The local accumulation
196 of PIP2 is essential to initiate the polymerization of filamentous actin (F-actin), a process that
197 drives extension of the leading edges of the nascent phagosome around the particle (*24*). However,

198 to complete the engulfment and internalization of the particle, F-actin must disassemble at the base
199 of the phagocytic cup. This is achieved through a local conversion of PIP2 into
200 phosphatidylinositol-3,4,5-*tris*phosphate (PIP3) by the phosphatidylinositol 3-kinase (PI3K;
201 Figure 5A) (*4*, *24*).
202
203 To determine whether blocking sphingolipid biosynthesis perturbs phagocytic signaling events
204 downstream of pathogen receptor activation, we first focused on the activation and localization of
205 the Rho GTPases Rac1 and Cdc42 in Zymosan A-treated wild type and Sptlc2$^{-/-}$ RAW 264.7 cells.
206 Visualization of activated Rho GTPases was enabled by transfecting cells with a fluorescent
207 biosensor comprising YFP fused to the p21-binding domain of the p21-activated kinase PAK
208 (PBD(PAK)-YFP) (*24*, *25*). Twenty-four hours post transfection, cells were infected with
209 Zymosan A particles at an MOI of 10 and subjected to live cell imaging. In wild type cells, we
210 observed a sharp increase in PBD(PAK)-YFP fluorescence at the particle contact site.
211 Fluorescence levels peaked during particle engulfment, corresponding to the expected pattern of
212 pathogen-induced Rac1/Cdc42 activation (Figure 5B and 5C; Movie 1). In Sptlc2$^{-/-}$ cells, we also
213 observed an increase in PBD(PAK)-YFP fluorescence upon particle recognition. However, the
214 PBD(PAK)-YFP fluorescence intensity failed to reach the levels detected in Zymosan A-treated
215 wild type cells and faded out prior to a successful particle internalization, suggesting that Sptlc2$^{-/-}$
216 cells are impaired in particle-induced activation of Rho GTPases (Figure 5B and 5C; Movie 2).
217
218 We next visualized F-actin dynamics in Zymosan A-treated wild type and Sptlc2$^{-/-}$ cells using
219 LifeAct-GFP (*26*). In wild type cells, LifeAct-GFP was readily recruited to the particle contact
220 site. During particle engulfment, LifeAct-GFP accumulated at the leading edges of the phagosome

221 while disappearing from the base of the phagocytic cup (Figure 5D and 5E; Movie 3). In Sptlc2$^{-/-}$
222 cells, LifeAct-GFP was readily recruited to the particle contact site yet remained associated with
223 the base of the phagocytic cup and failed to accumulate at the leading edges of the nascent
224 phagosome (Figure 5D and 5E; Movie 4). From this we conclude that a block in sphingolipid
225 biosynthesis severely disrupts phagocytosis-associated F-actin dynamics, presumably causing the
226 uptake defect.
227
228 **Phosphoinositide turnover is impaired in Sptlc2$^{-/-}$ cells**
229 As PIP2 and PIP3 are key regulators of F-actin dynamics during phagocytosis (Figure 5A), we
230 next monitored the spatial distribution of these phosphoinositides in Zymosan A-treated wild type
231 and Sptlc2$^{-/-}$ cells. To this end, cells were first transfected with a GFP-fusion of the plekstrin
232 homology (PH) domain of the phospholipase C-delta (PH(PLCδ)-GFP), which serves as a
233 fluorescent biosensor for PIP2 (*4*, *27*). In Zymosan A-treated wild type cells, PH(PLCδ)-GFP was
234 readily concentrated at the particle contact site and preferentially accumulated at the leading edges
235 of the nascent phagosome during particle engulfment (Figure 5F and 5G; Movie 5). In Sptlc2$^{-/-}$
236 cells, however, PH(PLCδ)-GFP was readily recruited to the contact site but remained associated
237 with the base of the phagocytic cup, analogous to what we observed with the LifeAct-GFP probe.
238 This suggests PIP2 synthesis is initiated upon Zymosan A binding, but that PIP2 turnover at the
239 base of the phagocytic synapse is impaired in Sptlc2$^{-/-}$ cells (Figure 5F and 5G; Movie 6).
240
241 To check whether a block in sphingolipid biosynthesis affects the turn-over of PIP2 into PIP3 in
242 Zymosan-A-treated cells, wild type and Sptlc2$^{-/-}$ RAW 264.7 cells were transfected with a GFP-
243 fusion of the PH domain of Akt (PH(AKT)-GFP), which serves as a fluorescent biosensor for PIP3

244 (*4*, *27*). In wild type cells, PH(AKT)-GFP was readily recruited to the particle contact site, and its
245 membrane association increased sharply during particle engulfment (Figure 5H and 5I; Movie 7).
246 In contrast, Sptlc2$^{-/-}$ cells almost completely failed to mobilize PH(AKT)-GFP at the particle
247 contact site (Figure 5F and 5G; Movie 8). Together, these results indicate that blocking
248 sphingolipid biosynthesis disrupts phosphoinositide metabolism at phagocytic synapses in
249 Zymosan A-treated macrophages, notably at the level of PIP2-to-PIP3 conversion, a step known
250 to be critical for the internalization of pathogenic bacteria by professional phagocytes (*24*).
251

252 **Production of sphingomyelin, not glycosphingolipids, is critical for efficient Mtb uptake**

253 Both sphingomyelin and glycosphingolipids are highly enriched in the exoplasmic leaflet of the
254 plasma membrane of mammalian cells. Therefore, we next addressed whether efficient phagocytic
255 uptake of Mtb relies on the production of sphingomyelin, glycosphingolipids, or both. Bulk
256 production of sphingomyelin is mediated by the enzyme sphingomyelin synthase 1 (SGMS1) in
257 the *trans*-Golgi whereas glycosphingolipid production is strictly dependent on the enzyme UDP-
258 glucose ceramide glycosyltransferase (UGCG) in the *cis*-Golgi (*9*, *28*). We used CRISPR/Cas9
259 gene editing to ablate UGCG expression in THP-1 cells (Supplemental Figure 3), and the lab of
260 Dr. Virriera-Winter kindly provided us with SGMS1 knockout U937 cells (*14*). Strikingly, SGMS1
261 knockout resulted in a major (~60%) reduction in the phagocytic uptake of mCherry-expressing
262 Mbt by U937 cells (Figure 6A and 6B), similar to what we observed in myriocin or FB1-treated
263 U937 cells (Figure 2H and 2I). In contrast, genetic ablation of UGCG had no impact on Mtb uptake
264 by THP-1 cells (Figure 6C and 6D), even though phagocytosis of Mtb in THP-1 cells can be readily
265 inhibited by myriocin and FB1 (Figure 2F and 2G). Together, these data indicate that an efficient

266 uptake of Mtb by professional phagocytes is critically dependent on an intact sphingomyelin
267 biosynthetic pathway whereas the production of glycosphingolipids is dispensable for this process.
268

269 **Discussion**

270 In this study, we report that the invasion of phagocytes by Mtb is critically dependent on an intact
271 sphingolipid biosynthetic pathway. Blocking sphingolipid production does not affect
272 macropinocytosis of Herpes Simplex Virus, indicating that phagocytes remain susceptible to
273 infection by pathogens that utilize other routes of cellular uptake. Strikingly, sphingolipid
274 biosynthetic Sptlc2$^{-/-}$ mutant cells display normal pathogen-induced clustering of phagocytic
275 receptors, yet fail to exclude the regulatory phosphatase CD45 from the phagocytic synapse. We
276 also show that key steps in the downstream signaling cascade, notably Rho GTPase activation and
277 phosphoinositide turnover, are significantly impaired in the mutant cells, leading to perturbations
278 in actin dynamics and defective phagosome formation. Blocking production of sphingomyelin, not
279 glycosphingolipids, suffices to disrupt phagocytic uptake of Mtb. While it remains to be
280 determined if this class of lipids plays a role in intracellular bacterial replication and disease
281 outcome *in vivo*, our findings disclose a vital role of sphingomyelin metabolism in an early step of
282 Mtb invasion.
283

284 A major finding of this work is that macrophages defective in sphingolipid biosynthesis are unable
285 to segregate CD45 from pathogen-induced clusters of Dectin-1 at the phagocytic cup. Dectin-1
286 belongs to a family of phagocytic cell surface receptors that initiate internalization of pathogens,
287 including Mtb (*7*, *29*). Upon pathogen engagement, these receptors cluster in the lateral plane of
288 the membrane, bringing their cytosolic domains in close apposition (*7*). The cytosolic domain of

289 Dectin-1 contains an immunoreceptor tyrosine-based activation motif (ITAM), which becomes
290 phosphorylated by Src and Syk family kinases upon receptor coalescence (*30*). Importantly,
291 segregation of the regulatory tyrosine phosphatase CD45 from the site of Dectin-1 clustering is a
292 crucial step in the amplification of a downstream phosphorylation cascade (*7*), which eventually
293 culminates in the recruitment of phosphoinositide-modifying enzymes including the
294 phosphoinositide 3-kinase (PI3K) (*4*, *31*). Thus, our finding that Sptlc2$^{-/-}$ cells fail to generate PIP3
295 at the phagocytic cup might be due to an impaired phagocyte receptor signaling caused by a
296 defective segregation of CD45. PI3K activation and formation of PIP3 at the pathogen engagement
297 site are necessary for late stages of pseudopodia progression, the clearance of actin at the base of
298 the phagocytic cup, and phagosome closure (*4*). Collectively, our data suggest that blocking
299 sphingolipid biosynthesis affects the phagocytic uptake of Mtb by precluding a proper activation
300 of phagocyte receptors during pathogen engagement.
301
302 Another key observation is that production of sphingomyelin rather than sphingolipid biosynthesis
303 *per se* is critical for efficient phagocytic uptake of Mtb. Sphingomyelin is a dominant sphingolipid
304 in the plasma membrane of mammalian cells. Owing to its saturated nature and hydrogen-bonding
305 capacity, sphingomyelin enables the formation of cholesterol/sphingolipid-enriched microdomains
306 (*32*). In this capacity, sphingomyelin may serve a critical role in the lateral organization and
307 activation of signaling complexes that promote Mtb invasion, consistent with prior reports that
308 cholesterol is essential for Mtb entry into macrophages (*33*). However, an alternative scenario is
309 that a sphingomyelin-derived metabolite, ceramide, facilitates the phagocytic uptake of Mtb.
310 Previous work revealed that hydrolysis of cell surface sphingomyelin by acid sphingomyelinase
311 mediates the invasion of gram-negative pathogens like *Neisseria gonorrhoeae* and *Pseudomonas*

312 *aeruginosa* in mammalian cells (*34*, *35*). Activation of acid sphingomyelinase at the pathogen
313 contact site appears to trigger local assembly of ceramide-enriched signaling platforms that initiate
314 internalization (*36*). While sphingomyelinases and ceramides have also been implicated in
315 mycobacterial infection (*37*, *38*), the underlying molecular principles remain to be explored.
316
317 In sum, we show that Mtb relies on an intact sphingomyelin biosynthetic pathway to efficiently
318 invade professional phagocytes. While the latter process is critical for the clearance of pathogens,
319 Mtb harnesses phagocytosis to gain entry to the host cells and establish long-term survival. By
320 providing fresh insights into the underlying mechanisms, our study makes a significant
321 contribution to the development of new strategies to fight this ancient pathogen.
322
323

324 **Materials and Methods**

325

326 **Reagents**

327 Myriocin and FB1 were purchased from Cayman Chemical Company. 3-L-[^{14}C]-serine was
328 purchased from American Radioactivity. Phorbol 12-myristate 13-acetate (PMA) was purchased
329 from BioLegend. 4% paraformaldehyde was purchased from Fisher Scientific. DyLight® 488
330 Phalloidin was purchased from Cell Signaling Technology, and Alexa Fluor 647-conjugated
331 Zymosan A (*S. cerevisiae*) BioParticles were purchased from Thermo Fisher. Mouse Monoclonal
332 antibody against GAPDH (ab8245) was purchased from Abcam. Anti-rabbit IgG HRP-linked
333 antibody and anti-mouse IgG HRP-linked antibody were purchased from Cell Signaling. APC-
334 conjugated, rat monoclonal antibody against CD45 antibody (Clone 30-F11) was purchased from
335 Biolegend. FITC-conjugated, rat monoclonal antibody against Dectin-1 (Clone 2A11) was
336 purchased from AbD Serotec. Zombie Aqua™ Fixable Viability Kit (part #77143) was purchased
337 from BioLegend.

338

339 **Plasmids**

340 The plasmids used for generation of lentivirus consists of the pCDH-CMV(-)-sgRNA plasmid, the
341 psPAX2 (packaging) and pMD2.G (envelope) plasmids. pCW-Cas9 lentivirus was purchased from
342 Addgene. The pMXsIP-Dectin-1-GFP was kindly provided by the lab of Dr. Hidde Ploegh (Boston
343 Children's Hospital, Boston, MA) (*7*). Active (GTP-bound) Rac1/Cdc42 was detected with
344 PAK(PBD)-YFP, a plasmid encoding the PBD of PAK fused to YFP was obtained from Addgene
345 (*25*). PI(4,5)P2 was detected with PH(PLCδ)-GFP, a plasmid encoding the PH domain of PLCδ
346 fused to GFP. PI(3,4,5)P3 levels were monitored by PH(AKT)-GFP, a plasmid encoding the PH

347 domain of AKT fused to GFP (*39*). These two fusion constructs were kindly provided by the lab
348 of Dr. Hidde Ploegh (Boston Children's Hospital, Boston, MA).
349
350 **Cell culture and small molecule inhibitor treatment**
351 THP-1, U937, and DC2.4 cells were routinely cultured in RPMI medium supplemented with 10%
352 FBS (Seradigm) and 1% Pen Strep (Gibco). RAW 264.7 cells were cultured in DMEM
353 supplemented with 10% FBS and 1% PenStrep. All cell lines were cultured at 37 °C and 5% CO_2.
354 In plating adherent cells (RAW 264.7 and DC2.4), cells were lifted using 0.25% trypsin solution
355 (Gibco) and counted using hemocytometer, with Trypan Blue solution (Gibco) for counterstain.
356 THP-1 and U937 cells were differentiated to macrophages by 50ng/ml PMA for 1 day in RPMI
357 medium supplemented with 10% FBS, after which the cells were treated with 5μM myriocin or
358 FB1 for 3 days in RPMI supplemented with 10% FBS and 1%Pen Strep. RAW 264.7 and DC2.4
359 cells were treated similarly with myriocin and FB1 – however, 24-hours before infection, cells
360 were lifted and counted, and seeded at appropriate density in 96-well plates or on coverslips.
361 Biological replicates represent independent treatments with chemical inhibitors and infections on
362 separate days.
363
364 **Metabolic labeling and thin layer chromatography**
365 $5x10^5$ cells were seeded into a 6-well plate. Cells were labeled with 1μCi/ml of 3-L-[^{14}C]-serine
366 for 4 hours in Opti-MEM supplemented with the appropriate inhibitors. Cells were then washed
367 two times with PBS and lipid extraction was done following the Bligh and Dyer method (*40*). The
368 methanol/chloroform-lipid extracts were dried by nitrogen gas. Dried lipids were re-dissolved in
369 several drops of chloroform/methanol (1:2, vol/vol) and loaded on a TLC plate. Lipids were

370 separated by developing the TLC plate first in acetone and then in a mixture of chloroform,
371 methanol and 25% ammonia solution (50:25:6, vol/vol/vol). Radiolabeled lipids were detected on
372 a Storm 825 Phosphor-Imager (GE Healthcare).
373
374 **Lipodomics**
375 LC-MS/MS analysis was performed as described previously (*41*). Lipids were extracted from lysed
376 RAW 246.7 cells according to 50µg of protein by chloroform/methanol extraction1. Before the
377 extraction a standard mix containing Sphingosine (d17:1), Ceramide (d18:1/17), Glycosyl(ß) (C12
378 Cer) and Sphingomyelin (17:0) was spiked into each sample for normalization and quantification.
379 The dried lipid films were dissolved in mixture of mobile phase A (60:40 water/acetonitrile,
380 including 10 mM ammonium formate and 0.1% formic acid) and mobile phase B (88:10:2 2-
381 propanol/acetonitrile/H20, including 2 mM ammonium formate and 0.02% formic acid) with a
382 ratio of 65:35. HPLC analysis was performed using a C30 reverse-phase column. (Thermo
383 Acclaim C30, 2.1 × 250 mm, 3 µm, operated at 50° C; Thermo Fisher Scientific) connected to an
384 HP 1100 series HPLC (Agilent) HPLC system and a QExactivePLUS orbitrap mass spectrometer
385 (Thermo Fisher Scientific) equipped with a heated electrospray ionization (HESI) probe. The
386 elution was performed with a gradient of 45 min; during 0–3 min, elution starts with 40% B and
387 increases to 100%; in a linear gradient over 23 mins. 100% B is maintained for 3 mins. Afterwards
388 solvent B was decreased to 40% and maintained for another 15 min for column re- equilibration.
389 The flow-rate was set to 0.1 ml/min. MS spectra of lipids were acquired in full-scan/data-
390 dependent MS2 mode. The maximum injection time for full scans was 100 ms, with a target value
391 of 3,000,000 at a resolution of 70,000 at m/z 200 and a mass range of 200–2000 m/z in both,
392 positive and negative mode. The 10 most intense ions from the survey scan were selected and

393 fragmented with HCD with a normalized collision energy of 30. Target values for MS/MS were
394 set at 100,000 with a maximum injection time of 50 ms at a resolution of 17,500 at m/z 200. To
395 avoid repetitive sequencing, the dynamic exclusion of sequenced lipids was set at 10 s. Peaks were
396 analyzed using the Lipid Search algorithm (MKI, Tokyo, Japan). Peaks were defined through raw
397 files, product ion and precursor ion accurate masses. Candidate molecular species were identified
398 by database (>1,000,000 entries) search of positive (+H+; +NH4+) ion adducts. Mass tolerance
399 was set to five ppm for the precursor mass. Samples were aligned within a time window and results
400 combined in a single report. From the intensities of lipid standards and lipid classes absolute values
401 for each lipid in pmol/mg protein were calculated.
402
403 **Generation of lentiviruses**
404 Lentivirus production was performed as described previously (*42*). Briefly, lentiviruses were
405 produced by co-transfection of HEK 293T cells with the lentiviral vectors that contain our gene of
406 interest (pCDH-sgRNA or pCW-Cas9) and the packaging plasmids (psPAX2 and pMD2.G).
407 Transfection was performed with Lipofectamine 3000 (Thermo Fisher) according to
408 manufacturer's instructions. Cells were cultured in DMEM supplemented with 10%FBS and the
409 growth medium was replaced after 6 hours. 48 hours after transfection, lentivirus-containing
410 supernatants were harvested, centrifuge for 5min at 1250 rpm and filtered through a 0.45μm filter.
411
412 **Generation of CRISPR/Cas9-mediated knockout cell lines**
413 CRISPR/Cas9-mediated genome-editing for genes involved in the sphingolipid pathway were
414 performed as described previously (*15*). Briefly, to generate Sptlc2$^{-/-}$ knockout RAW 264.7 cells
415 were infected with lentivirus (pCW-Cas9) encoding Cas9 cDNA, and were cultured in media

416 containing 2 μg/mL of puromycin (Sigma Aldrich). The following two seed sequences (CRISPR
417 target sequences) preceding PAM motifs found in the open reading frame of Sptlc2 gene were
418 used: Sptlc2 #1 GAACGGCTGCGTCAAGAAC; Sptlc2 #2: AGCAGCACCGCCACCGTCG.
419 The CRISPR target sequence for UGCG was as follows: GCTGTGGCTGATGCATTTCA.
420 Potential off-target effects of the seed sequence were evaluated using the NCBI Mus musculus
421 Nucleotide BLAST. Generation of CRISPR/Cas9-mediated Sptlc2-knockout RAW 264.7 cell line
422 and UGCG-knockout THP-1 cell line were performed as previously described (*42*). Briefly,
423 CRISPR gBlock was designed to clone into the restriction enzymatic site NheI/BamHI of pCDH-
424 CMV(-) (SBI; CD515B-1) as follows:
425 cacagtcagacagtgactcaGTGTCACAgctagcTTTCCCATGATTCCTTCATATTTGCATATACGA
426 TACAAGGCTGTTAGAGAGATAATTAGAATTAATTTGACTGTAAACACAAAGATATTA
427 GTACAAAATACGTGACGTAGAAAGTAATAATTTCTTGGGTAGTTTGCAGTTTTAAAA
428 TTATGTTTTAAAATGGACTATCATATGCTTACCGTAACTTGAAAGTATTTCGATTTCT
429 TGGCTTTATATATCTTGTGGAAAGGACGAAACACCGnnnnnnnnnnnnnnnnnnnGTTTTAG
430 AGCTAGAAATAGCAAGTTAAAATAAGGCTAGTCCGTTATCAACTTGAAAAAGTGGC
431 ACCGAGTCGGTGCTTTTTTTggatccTGTGCACAgtcagtcacagtcagtctac (n: CRISPR target
432 sequences).
433
434 The gBlock was then digested using the restriction enzymes NheI and BamHI and ligated into
435 pCDH-CMV(-) vector that was linearized by digesting with the same restriction enzyme. The
436 Cas9-inducible cells were infected with lentivirus carrying pCDH-CMV(-)-sgRNA, and were
437 cultured in media containing 250 μg/mL of hygromycin B (Life Technology). To induce
438 expression of Cas9, cells were treated with 1 μg/mL of doxycycline (Clontech) for 3–5 days.

439 Clonal selection was performed by single cell dilution on 96-well plates. The individual colonies
440 were collected and the expression of Sptlc2 was examined by western-blotting using Sptlc2
441 antibody. U937 SGSM1$^{-/-}$ cells were kindly provided by Dr. Arturo Zychlinsky (Max Planck
442 Institute of Biochemistry, Berlin, Germany) and the CRISPR/Cas9-mediated knock out cell lines
443 were established as described in Winter et al., 2016 (*14*).
444
445 **Culturing of Mtb**
446 Culturing and infection of Mtb was conducted in a Biosafety-level 3 laboratory following general
447 safety guidelines. Mtb strain H37R, expressing constitutively mCherry were obtained from the
448 Fortune lab (Ragon Institute, Cambridge, MA). It was cultured at 37°C in 7H9 Broth medium
449 supplemented with 50µg/ml hygromycin B. The density of the bacteria at the time of infection is
450 between OD600 of 0.6 - 0.8.
451
452 **Mtb uptake assay**
453 For infection of THP-1 and U937 cells, the cells were seeded into a SensoPlate™ 96-Well Glass-
454 Bottom Plates (Greiner Bio-One) at a density of $1.5x10^4$ cells per well in RPMI supplemented with
455 10% FBS, 1% PenStrep and 50ng/ml PMA at 37°C. One day after differentiation, cells were
456 treated for 3 days with 5µM myriocin or 15µM FB1. These cells were then infected with a
457 multiplicity of infection (MOI) of 10 in RPMI supplemented with 10% FBS for 2 hours at 37°C.
458 For infection of RAW 264.7 and DC2.4 cells, $2.0x10^4$ cells per well were seeded into a
459 SensoPlate™ 96-Well Glass-Bottom Plates (Greiner Bio-One). 24 hour later, the cells were
460 infected with an MOI of 10 in RPMI supplemented with 10% FBS for 2 hours at 37°C. Cells were
461 washed with PBS, and then fixed with 4% PFA over night at 4°C.

462

463 **Phagocytosis measurement assay**

464 Fixed cells were washed twice with PBS and incubated for 15 min in Permeabilization Buffer
465 (0.1% Triton X-100 and 1%BSA). Cells were stained with Phalloidin-Alexa 488 (Thermo Fisher)
466 at a final concentration of 33nM in permeabilization buffer for 60 min and washed one time with
467 PBS. After the Phalloidin-staining, cells were stained with DAPI for 10 mins and washed 3 times
468 with PBS. Cells were then imaged using the Keyence BZ-X700 with a PlanFluor 20x objective.
469 The parameters for imaging were kept the same for each sample. For image analysis the Keyence
470 BZ-X Analyzer software was used. In brief: The outline of the cells was determined via the
471 Alexa488 signal (Phalloidin staining) and the number and area of mCherry (Mtb) signal in the
472 Alexa488 signal was detected by the program. In a second round the number of cells was
473 determined by counting the nuclei via the DAPI staining. Number of bacteria (mCherry-signal)
474 inside the cell was divided by the number of cells (DAPI signal) to identify the phagocytosis
475 efficiency.

476

477 **Herpes Simplex Virus-1 infection**

478 HSV-1-mCherry reporter virus was kindly provided by the lab of Dr. David Johnson (Oregon
479 Health and Science University, Portland, Oregon). Twenty-four hours prior to infection, $1x10^4$
480 wild type and Sptlc2 knockout RAW 264.7 cells were seeded on glass coverslips in a 12-well plate.
481 Cells were equally infected at an MOI ~1, and incubated for 12 hours at 37°C and 5% CO_2.
482 Coverslips were fixed for 20 mins in 4% paraformaldehyde, stained with DAPI and then imaged
483 on a Keyence BZ-X700. Infection rates were calculated by dividing the mCherry expressing cells
484 with the total number of cells (DAPI signal).

485

486 **Live imaging of phagocytosis**

487 For transient transfection, RAW 264.7 cells were seeded into a SensoPlate™ 96-Well glass-bottom
488 plates at a cell number of $1.0x10^4$ cells/well 24 hours prior transfection. Transfection was
489 conducted with Lipofectamine 3000 according to manufacturer's instructions. For imaging, the
490 growth medium was aspirated and replaced with RPMI without phenol red containing Zymosan A
491 Bioparticles Alexa595 at an MOI of 10. The 96-well plates were centrifuged at 1000rpm for one
492 minute. The cells were imaged with the SDC microscope (Nikon) and 3-4 different spots per well
493 were imaged at the same time for 60 min with capture intervals of 15 sec. The parameters for
494 imaging were kept the same for each sample.

495

496 **Live image analysis (quantification)**

497 Of live cell images, individual images were selected for further analysis if they captured a cell
498 bound to a Zymosan particle while maintaining a healthy morphology throughout the imaging
499 time-course. Imaging analysis was performed using FIJI software. The parameters for image
500 processing were kept constant when comparing different data sets. The area of the phagosome was
501 selected, cropped and opened in a new window. The threshold at different time points was
502 measured by the analyze-measure function of FIJI. The values for the GFP-threshold of the
503 phagosome area were divided by the values for the GFP-threshold of the whole cell at the
504 corresponding time points.

505

506 **Dectin-1 and CD45 displacement assay**

507 RAW 264.7 WT and Sptlc2$^{-/-}$ cells were seeded on glass coverslips in 12-well plates and grown to
508 70-90% confluency overnight. Cells were transfected with pMXsIP Dectin-1-GFP using
509 Lipofectamine 3000 (Invitrogen) according to the manufacturer's instructions. After 24 hrs, cells
510 were washed three times with ice-cold PBS, kept on ice for 5 min, and inoculated with Alexa Fluor
511 594-conjugated Zymosan A in chilled serum-free DMEM at a ratio of 10 beads per cell. After
512 centrifugation for 5 min at 250 x g and 4°C, cells were incubated for 2 min at 37°C, washed three
513 times with ice-cold PBS to remove unbound Zymosan, then fixed for 15 min with 4%
514 paraformaldehyde. Images were collected using an LSM880 confocal microscope using a PLAN
515 APO 63x oil-immersion objective and AIRY SCAN. Image analysis was performed using FIJI.
516 Briefly, a region-of-interest was defined around the Zymosan particle, and Pearson's correlation
517 coefficient between Dectin-1-GFP signal and anti-CD45-APC signal was calculated using the
518 colocalization function.
519
520 **Flow cytometry**
521 RAW 264.7 wild type and Sptlc2$^{-/-}$ cells were rinsed with PBS and lifted from the flask using
522 treatment with trypsin. Fc receptor was blocked with CD16/32 antibody (1:100) and cells were
523 stained with ZombieAqua Live/Dead (1:200). Cells were then stained with either CD45-APC
524 (1:200), or Dectin-1-FITC (1:50) for 30 min. Finally, cells were fixed for 20 mins in 4%
525 paraformaldehyde and analyzed using an LSR-II flow cytometer. Cells independently stained with
526 ZombieAqua, CD45-APC, and Dectin-1-FITC were used for compensation. Analysis was
527 performed using FlowJo software.
528
529

530 **References**

531 1. "Global tuberculosis report 2018." (Geneva, 2018).

532 2. C. J. Queval, R. Brosch, R. Simeone, The Macrophage: A Disputed Fortress in the Battle
533 against Mycobacterium tuberculosis. *Front. Microbiol.* **8** (2017),
534 doi:10.3389/fmicb.2017.02284.

535 3. V. Korb, A. Chuturgoon, D. Moodley, Mycobacterium tuberculosis: Manipulator of
536 Protective Immunity. *Int. J. Mol. Sci.* **17**, 131 (2016).

537 4. R. Levin, S. Grinstein, D. Schlam, Phosphoinositides in phagocytosis and
538 macropinocytosis. *Biochim. Biophys. Acta - Mol. Cell Biol. Lipids*. **1851**, 805–823 (2015).

539 5. R. S. Flannagan, V. Jaumouillé, S. Grinstein, The Cell Biology of Phagocytosis. *Annu.*
540 *Rev. Pathol. Mech. Dis.* **7**, 61–98 (2012).

541 6. L. M. Stuart, R. A. B. Ezekowitz, Phagocytosis: Elegant complexity. *Immunity*. **22**, 539–
542 550 (2005).

543 7. H. S. Goodridge *et al.*, Activation of the innate immune receptor Dectin-1 upon formation
544 of a 'phagocytic synapse.' *Nature*. **472**, 471–475 (2011).

545 8. R. Pralhada Rao *et al.*, Sphingolipid Metabolic Pathway: An Overview of Major Roles
546 Played in Human Diseases. *J. Lipids*. **2013**, 1–12 (2013).

547 9. C. Gault, L. Obeid, Y. Hannun, An overview of sphingolipid metabolism: from synthesis
548 to breakdown Introduction to Sphingolipid Metabolism. *Adv Exp Med Biol*. **688**, 1–23
549 (2010).

550 10. T. A. Taha, T. D. Mullen, L. M. Obeid, A house divided: Ceramide, sphingosine, and
551 sphingosine-1-phosphate in programmed cell death. *Biochim. Biophys. Acta - Biomembr.*
552 **1758**, 2027–2036 (2006).

553 11. M. Kinoshita, K. G. N. Suzuki, M. Murata, N. Matsumori, Evidence of lipid rafts based on
554 the partition and dynamic behavior of sphingomyelins. *Chem. Phys. Lipids*. **215**, 84–95
555 (2018).
556 12. A. B. García-Arribas, A. Alonso, F. M. Goñi, Cholesterol interactions with ceramide and
557 sphingomyelin. *Chem. Phys. Lipids*. **199**, 26–34 (2016).
558 13. J. E. Carette *et al.*, Haploid Genetic Screens in Human Cells Identify Host Factors Used
559 by Pathogens. *Science (80-.).* **326**, 1231–1235 (2009).
560 14. S. Virreira Winter, A. Zychlinsky, B. W. Bardoel, Genome-wide CRISPR screen reveals
561 novel host factors required for Staphylococcus aureus α-hemolysin-mediated toxicity. *Sci.*
562 *Rep.* **6**, 24242 (2016).
563 15. F. G. Tafesse *et al.*, Disruption of Sphingolipid Biosynthesis Blocks Phagocytosis of
564 Candida albicans. *PLOS Pathog.* **11**, e1005188 (2015).
565 16. H. C. Leier, W. B. Messer, F. G. Tafesse, Lipids and pathogenic flaviviruses : An intimate
566 union, 1–7 (2018).
567 17. I. Meivar-Levy, H. Sabanay, A. D. Bershadsky, A. H. Futerman, The Role of
568 Sphingolipids in the Maintenance of Fibroblast Morphology. *J. Biol. Chem.* **272**, 1558–
569 1564 (2002).
570 18. T. W. Wisner, K. Sugimoto, P. W. Howard, Y. Kawaguchi, D. C. Johnson, Anterograde
571 Transport of Herpes Simplex Virus Capsids in Neurons by both Separate and Married
572 Mechanisms. *J. Virol.* **85**, 5919–5928 (2011).
573 19. C. Clement *et al.*, A novel role for phagocytosis-like uptake in herpes simplex virus entry.
574 *J. Cell Biol.* **174**, 1009–1021 (2006).
575 20. T. Gianni, V. Gatta, G. Campadelli-Fiume, V 3-integrin routes herpes simplex virus to an

576 entry pathway dependent on cholesterol-rich lipid rafts and dynamin2. *Proc. Natl. Acad.*
577 *Sci.* **107**, 22260–22265 (2010).
578 21. D. M. Underhill, Macrophage recognition of zymosan particles. *J. Endotoxin Res.* **9**, 176–
579 180 (2003).
580 22. M. Wagener, J. C. Hoving, H. Ndlovu, M. J. Marakalala, Dectin-1-Syk-CARD9 Signaling
581 Pathway in TB Immunity. *Front. Immunol.* **9** (2018), doi:10.3389/fimmu.2018.00225.
582 23. K. Simons, D. Toomre, Lipid rafts and signal transduction. *Nat. Rev. Mol. Cell Biol.* **1**,
583 31–39 (2000).
584 24. D. Schlam *et al.*, Phosphoinositide 3-kinase enables phagocytosis of large particles by
585 terminating actin assembly through Rac/Cdc42 GTPase-activating proteins. *Nat. Commun.*
586 **6**, 8623 (2015).
587 25. A. D. Hoppe, J. A. Swanson, Cdc42, Rac1, and Rac2 Display Distinct Patterns of
588 Activation during Phagocytosis. *Mol. Biol. Cell*. **15**, 3509–3519 (2004).
589 26. J. Riedl *et al.*, Lifeact: a versatile marker to visualize F-actin. *Nat. Methods*. **5**, 605–607
590 (2008).
591 27. J. G. Marshall *et al.*, Restricted Accumulation of Phosphatidylinositol 3-Kinase Products
592 in a Plasmalemmal Subdomain during Fcγ Receptor-Mediated Phagocytosis. *J. Cell Biol.*
593 **153**, 1369–1380 (2001).
594 28. M. S. Wegner, L. Gruber, P. Mattjus, G. Geisslinger, S. Grösch, The UDP-glucose
595 ceramide glycosyltransferase (UGCG) and the link to multidrug resistance protein 1
596 (MDR1). *BMC Cancer*. **18**, 1–10 (2018).
597 29. M. M. Hossain, M.-N. Norazmi, Pattern Recognition Receptors and Cytokines in
598 Mycobacterium tuberculosis Infection—The Double-Edged Sword? *Biomed Res. Int.*

599 **2013**, 1–18 (2013).

600 30. S. A. Woodcock *et al.*, Src-Induced Disassembly of Adherens Junctions Requires
601 Localized Phosphorylation and Degradation of the Rac Activator Tiam1. *Mol. Cell*. **33**,
602 639–653 (2009).

603 31. J. W. Zhu, T. Brdicka, T. R. Katsumoto, J. Lin, A. Weiss, Structurally Distinct
604 Phosphatases CD45 and CD148 Both Regulate B Cell and Macrophage Immunoreceptor
605 Signaling. *Immunity*. **28**, 183–196 (2008).

606 32. J. P. Slotte, Biological functions of sphingomyelins. *Prog. Lipid Res.* **52**, 424–437 (2013).

607 33. J. Gatfield, J. Pieters, Essential role for cholesterol in entry of mycobacteria into
608 macrophages. *Science*. **288**, 1647–50 (2000).

609 34. H. Grassmé *et al.*, Acidic sphingomyelinase mediates entry of N. gonorrhoeae into
610 nonphagocytic cells. *Cell*. **91**, 605–15 (1997).

611 35. C. Li *et al.*, Acid Sphingomyelinase-Ceramide System in Bacterial Infections. *Cell.*
612 *Physiol. Biochem.* **52**, 280–301 (2019).

613 36. H. Grassmé *et al.*, Host defense against Pseudomonas aeruginosa requires ceramide-rich
614 membrane rafts. *Nat. Med.* **9**, 322 (2003).

615 37. A. Speer *et al.*, Surface hydrolysis of sphingomyelin by the outer membrane protein
616 Rv0888 supports replication of M ycobacterium tuberculosis in macrophages. *Mol.*
617 *Microbiol.* **97**, 881–897 (2015).

618 38. G. Viswanathan, M. Jafurulla, G. A. Kumar, T. R. Raghunand, A. Chattopadhyay,
619 Macrophage sphingolipids are essential for the entry of mycobacteria. *Chem. Phys. Lipids*.
620 **213**, 25–31 (2018).

621 39. S. Feng *et al.*, A Rapidly Reversible Chemical Dimerizer System to Study Lipid Signaling

622 in Living Cells. *Angew. Chemie Int. Ed.* **53**, 6720–6723 (2014).

623 40. E. G. BLIGH, W. J. DYER, A rapid method of total lipid extraction and purification. *Can.*
624 *J. Biochem. Physiol.* **37**, 911–7 (1959).

625 41. C. S. Ejsing *et al.*, Global analysis of the yeast lipidome by quantitative shotgun mass
626 spectrometry. *Proc. Natl. Acad. Sci.* **106**, 2136–2141 (2009).

627 42. F. G. Tafesse *et al.*, GPR107, a G-protein-coupled Receptor Essential for Intoxication by
628 Pseudomonas aeruginosa Exotoxin A, Localizes to the Golgi and Is Cleaved by Furin. *J.*
629 *Biol. Chem.* **289**, 24005–24018 (2014).

630

631 **Acknowledgements**

632 This work was supported by the Medical Research Foundation and National Institutes of Health
633 (3R21AI124225-01A1) to F.G.T., and the Deutsche Forschungsgemeinschaft (Projects SFB944-
634 P14 and HO3539/1-1) to J.C.M.H. We would like to thank Dr. Hidde Ploegh (Boston Children's
635 Hospital, Boston, MA), Dr. Arturo Zychlinsky (Max Planck Institute of Biochemistry, Berlin,
636 Germany), and Dr. David Johnson (Oregon Health and Science University, Portland, OR) for
637 kindly providing reagents, cell lines, viruses, and plasmid constructs essential to the completion of
638 this study. We would also like to thank the members of the OHSU Advanced Light Microscopy
639 Core and the OHSU Flow Cytometry Shared Resource for assistance and training in data collection
640 and analysis – in particular, we would like to thank Dr. Stefanie Kaech Petrie, Matthew Lewis,
641 and Sara Christensen. We would finally like to thank Madeleine Faucher, Marie Foss, and Jossef
642 Osborn who kindly and patiently assisted in the editing and preparation of this work.

643 **Author Contributions**

644 P.N. and G.G. designed and performed the majority of experiments, and together prepared the
645 manuscript. H.L. optimized and performed fluorescent microscopy colocalization and assisted in
646 figure preparation. A.R., V.R., and F.P. created and characterized CRISPR knockout cell lines.
647 J.C.M.H. provided intellectual contributions in experimental design and data interpretation. F.G.T.
648 directed the research, interpreted the data, and edited the manuscript.
649
650 **Conflicts of interest**
651 The authors have no conflicts of interest to declare.
652

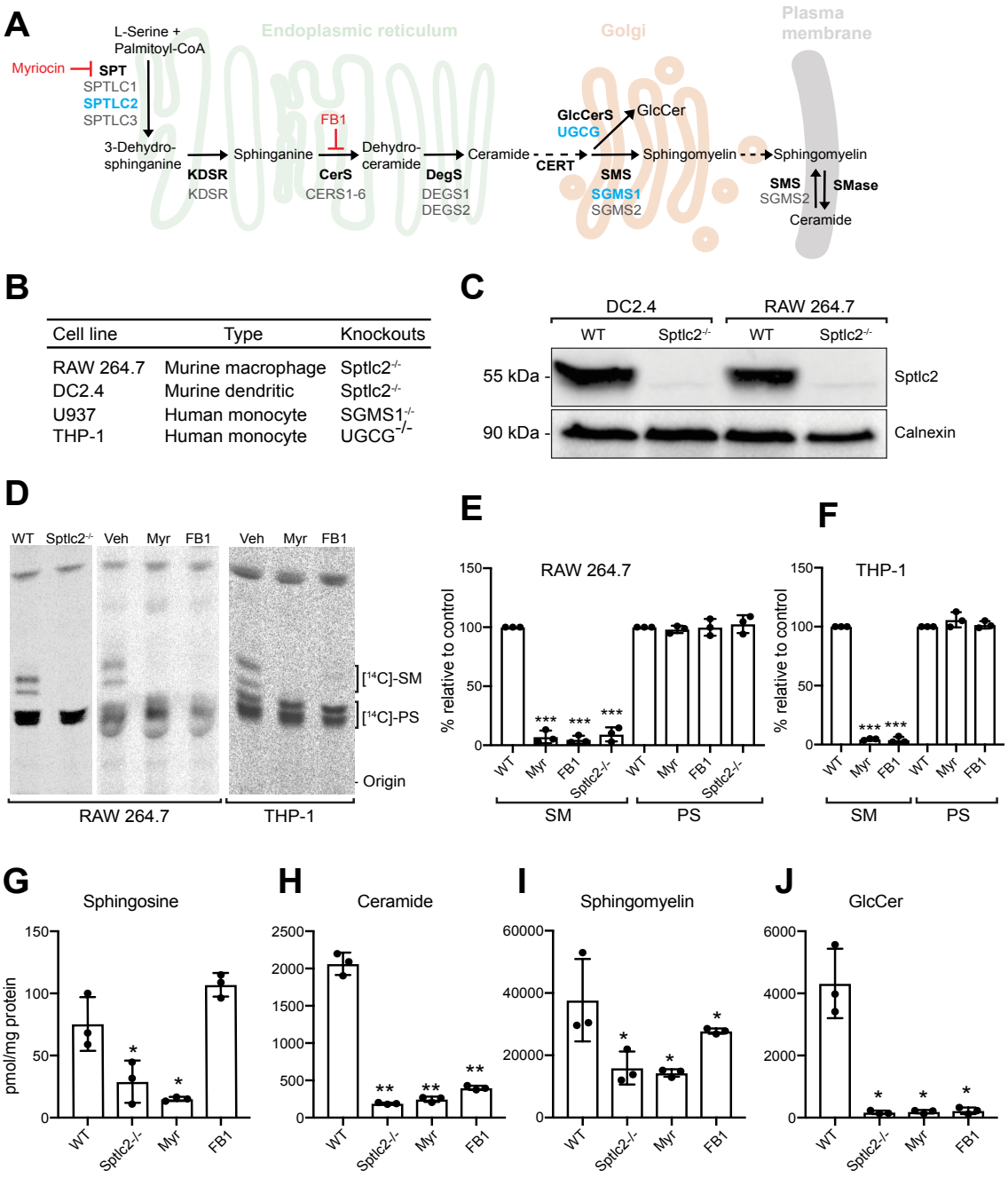

Figure 1: Manipulation of cellular sphingolipid levels using genetics and chemical tools. (A) Simplified overview of sphingolipid biosynthetic pathway. Genes that are deleted using CRISPR/Cas9 system in this study are indicated in blue and the inhibitors used in this study are shown in red. (B) Model phagocyte cell lines used in this study, respective species background, and genetic knockouts available. (C) DC2.4 and RAW 264.7 wild type and Sptlc2$^{-/-}$ cells were processed for immunoblotting with antibodies against Sptlc2 and Calnexin. (D) Control, Sptlc2$^{-/-}$ and inhibitor-treated cells were labeled with the sphingolipid precursor 3-L-[^{14}C]-serine, and total lipids were extracted and analyzed by thin layer chromatography (TLC) and autoradiography. (E, F) Quantification of the [^{14}C]-SM and [^{14}C]-PS signals from [^{14}C]-serine labeling of RAW 264.7 and THP-1 cells from TLC shown in *D*. (G-J) Total lipids were extracted from control, Sptlc2$^{-/-}$ and inhibitor-treated cells and lipid profiling was performed using LC/MS. Levels of sphingosine (G), ceramide (H), sphingomyelin (I) and glucosylceramide (GlucCer; J) are shown. All graphs display SD of three independent experiments, and an unpaired t-test was used to analyze the significance of the data. *p<0.05, **p<0.01, *** p < 0.001.

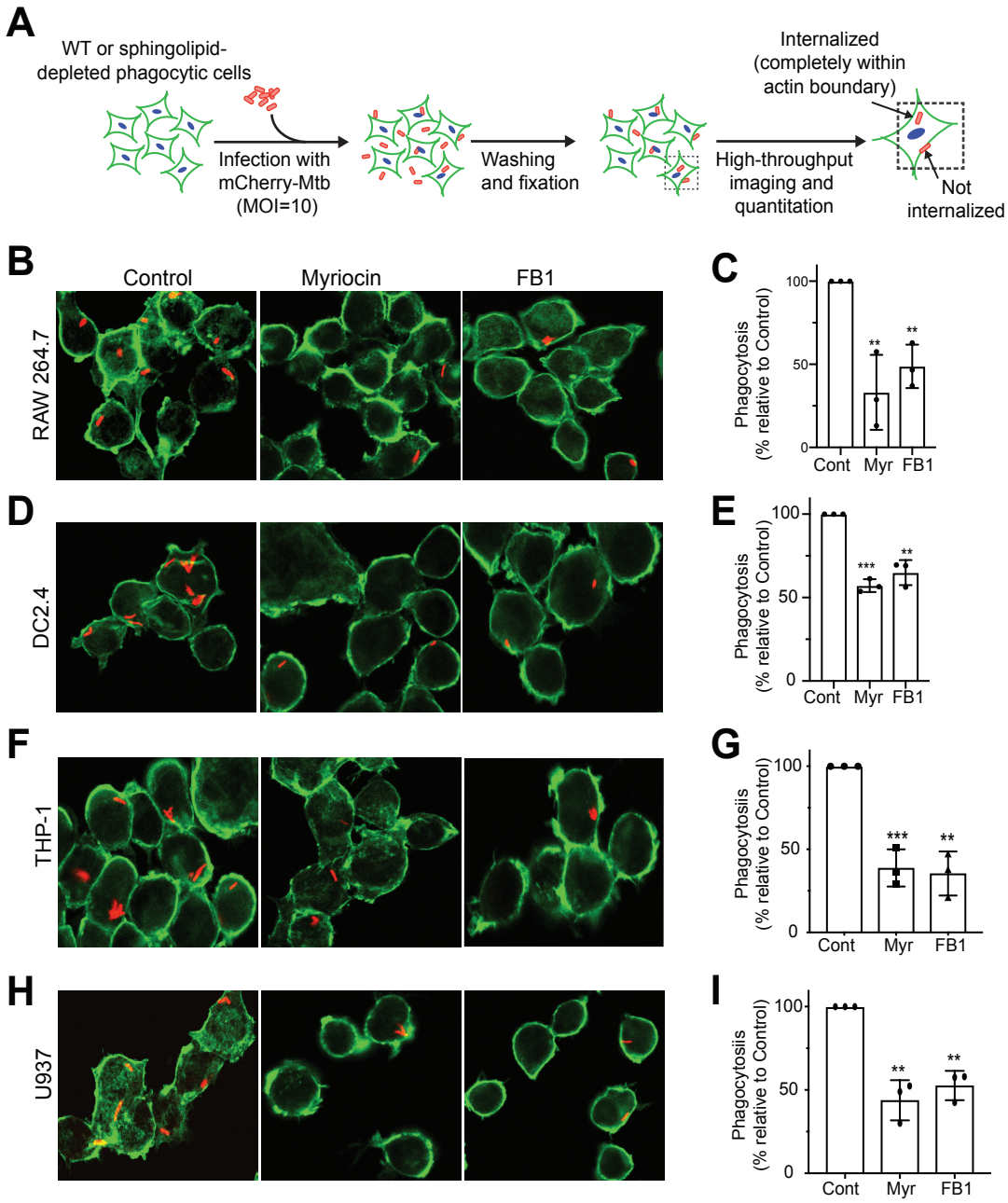

Figure 2: Sphingolipid biosynthesis is required for efficient phagocytosis of Mtb. (A) Overview of the phagocytosis experiment. Cells were infected with an mCherry-expressing Mtb and fixed after 2h. Cell outline was stained with Phalloidin A488 to differentiate between internalized and non-internalized Mtb and the nuclei was stained with DAPI to quantify the number of cells. (B, D) Representative images of Mtb-infected RAW 264.7 (B) and DC2.4 (D) cells. (C, E) Quantification of Mtb uptake in RAW 264.7 (C) and DC2.4 (E) cells. (E, H) Representative images of infected THP-1 (F) and U937 (H) monocyte-derived macrophages. (G, I) Quantification of Mtb uptake in THP-1 (G) and U937 (I) cells. All cell lines were treated for three days with myriocin or FB1. Three independent experiments were performed each in triplicate with at least 1,000 cells quantified per replicate. Mtb uptake was defined using total number of bacteria (mCherry signal) within cellular periphery (Phalloidin-Alexa488 signal) and cellular counts were defined by nuclear stain. Data are mean ± SD. ***p<0.001, two-tailed unpaired t-test. Data are mean ± SD. **p<0.01, ***p<0.001, two-tailed unpaired t-test.

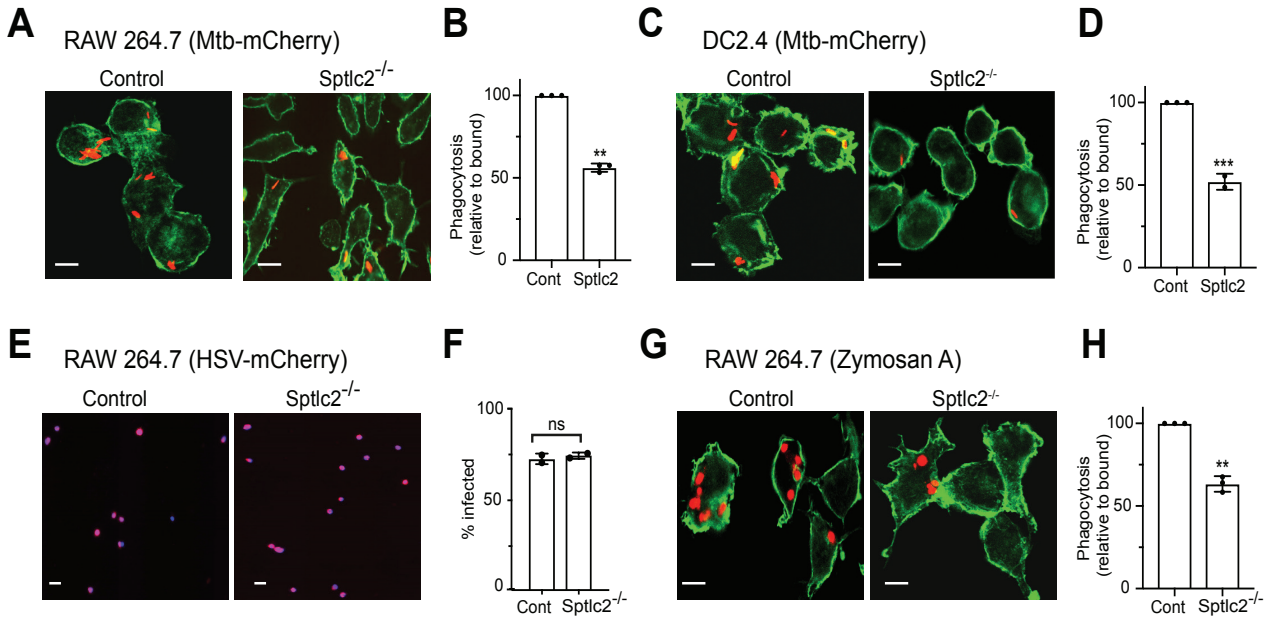

Figure 3: Sphingolipid biosynthesis is required for efficient phagocytosis of Mtb and Zymosan A, but not for HSV entry. (A) Representative images of wild type and Sptlc2$^{-/-}$ RAW 264.7 (A) and DC2.4 (C) cells infected with mCherry-expressing Mtb. (B, D) Quantification of Mtb uptake for experiments performed as in *A* and *C*, respectively. (E) Microscopy images of cells that were infected with HSV-mCherry (MOI of 1). At 12 h post infection, cells were fixed, stained with DAPI and analyzed by microscopy. (F) Quantification of experiments performed as described *E*. (G) Representative images of wild type and Sptlc2$^{-/-}$ RAW 264.7 cells infected with Alexa Fluor 594-conjugated Zymosan A particles. (H) Quantification of Zymosan A uptake performed as in *E*. Three independent experiments were performed each in triplicate with at least 1,000 cells quantified per replicate. Data are mean ± SD. ***p<0.001, two-tailed unpaired t-test. Data are mean ± SD. **p<0.01, ***p<0.001, ns = not significant, two-tailed unpaired t-test.

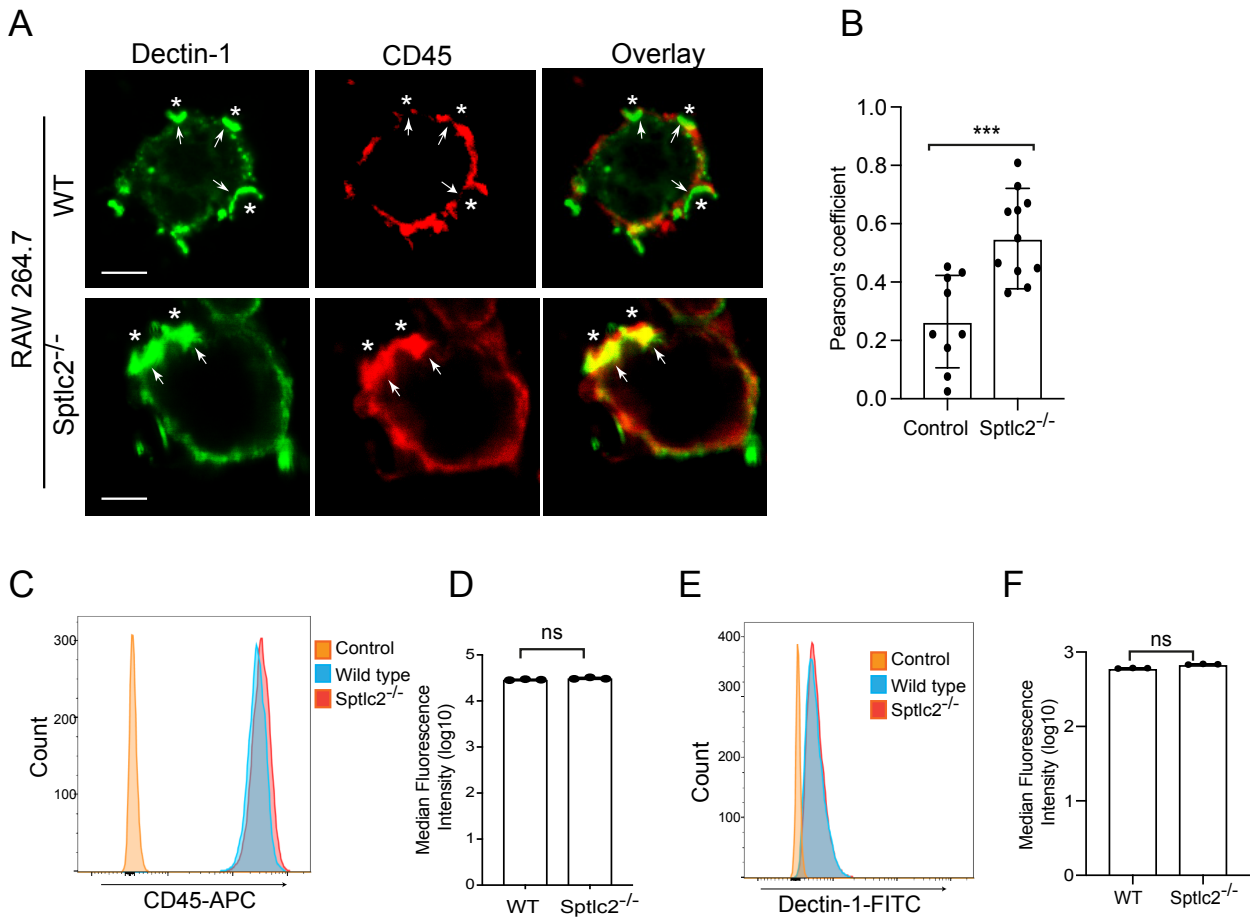

Figure 4: Exclusion of CD45 by Dectin-1 from the cup formation site is impaired in Sptlc2$^{-/-}$ cells. (A) Confocal microscopy of GFP-tagged Dectin-1-expressing RAW 264.7 macrophages stimulated with Zymosan A for 2 min and stained for CD45 (red). Zymosan particles are shown as star (*) at the phagocytic cup. (B) Colocalization measurement of CD45 and Dectin-1 at the site of cup formation as presented by Pearson's colocalization coefficient. (C, E) Flow cytometry of wildtype and Sptlc2$^{-/-}$ RAW 264.7 cells that were stained for CD45 and Dectin-1at the cell surface. (D, F) Graphs showing quantification of cell surface expression of the receptors described in *C* and *E*, respectively. All data are representative of 3 independent experiments performed in triplicate. Data are mean ± SD. ns = not significant, two-tailed unpaired t-test.

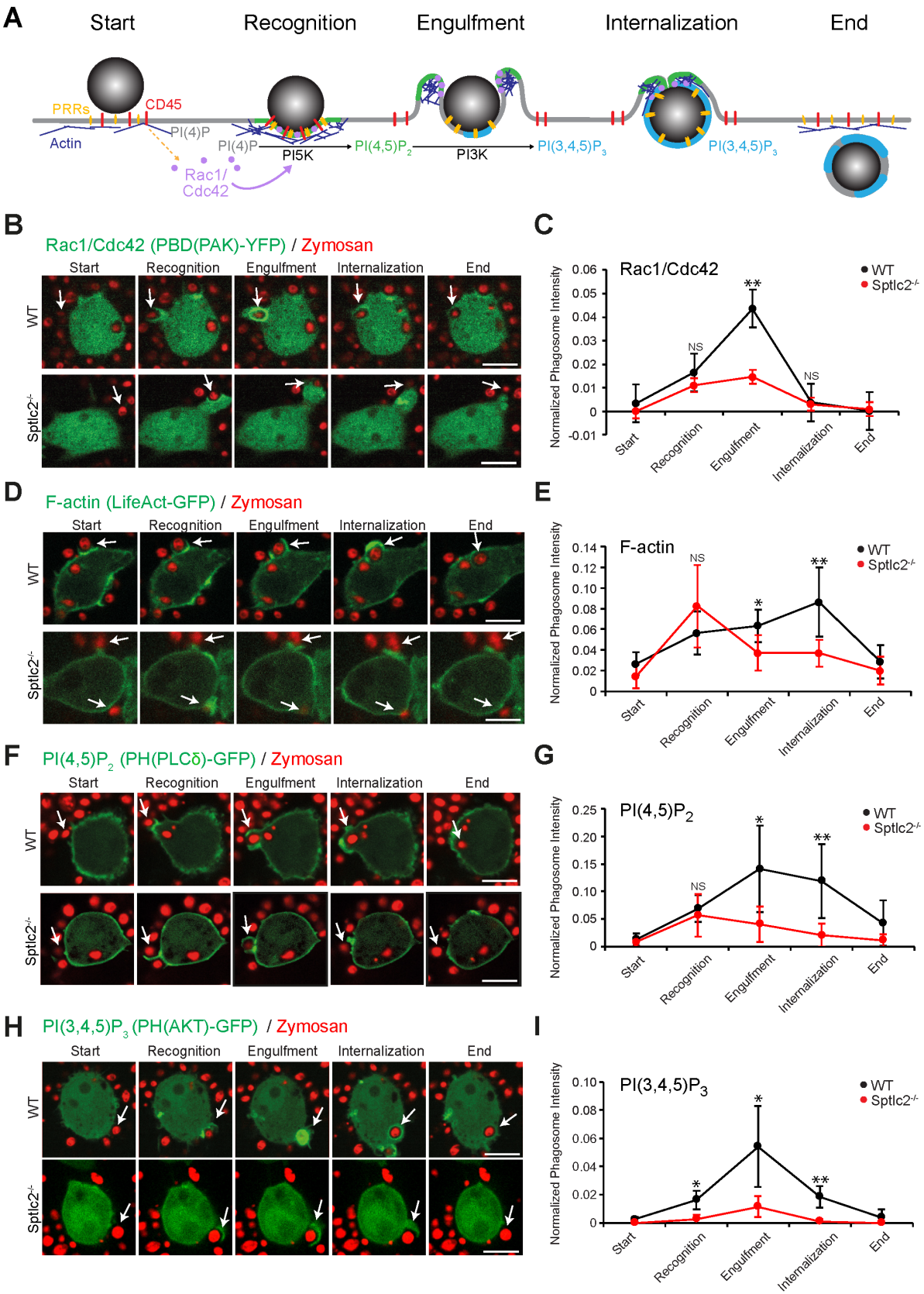
A
Start
Recognition
Engulfment
Internalization
End
PRRs
CD45
Actin
PI(4)P
PI(4)P
PI5K
PI(4,5)P2
PI3K
PI(3,4,5)P3
PI(3,4,5)P3
Rac1/
Cdc42
B
Rac1/Cdc42 (PBD(PAK)-YFP) / Zymosan
WT
Sptlc2-/-
C
Rac1/Cdc42
WT
Sptlc2-/-
Normalized Phagosome Intensity
NS
**
NS
D
F-actin (LifeAct-GFP) / Zymosan
E
F-actin
NS
*
**
F
PI(4,5)P2 (PH(PLCδ)-GFP) / Zymosan
G
PI(4,5)P2
NS
*
**
H
PI(3,4,5)P3 (PH(AKT)-GFP) / Zymosan
I
PI(3,4,5)P3
*
*
**

704

705 **Figure 5. Sphingolipids are essential for efficient phosphoinositide turnover at the phagocytic cup.**
706 (A) Schematic representation of the phagocytosis process. Upon pathogen engagement, pattern recognition
707 receptors (PRRs) cluster and displace CD45 phosphatase, thereby initiating the activation of the Rho
708 GTPases Cdc42 and Rac1, which in turn activate PI5K. This leads to a spatial production of PIP2 and F-
709 actin assembly. To permit phagosome progression, PI3K orchestrates the turnover of PIP2 to PIP3, leading
710 to F-actin disassembly at the base of the phagosome.
711 (B) Time-lapse confocal images of wild type and Sptlc2$^{-/-}$ RAW 264.7 cells transfected with PAK(PBD)–
712 GFP and infected with Zymosan Alexa Flour 594-conjugate at a MOI of 10. (C) Quantification of the
713 PAK(PBD) fluorescence intensity in the course of the formation of a phagocytic cup (shown in arrow) as
714 performed in *B*.
715 (D) Time-lapse confocal images of wild type and Sptlc2$^{-/-}$ RAW 264.7 cells transfected with LifeAct-GFP
716 and infected with Zymosan Alexa Flour 594-conjugate at a MOI of 10. (E) Quantification of the LifeAct
717 fluorescence intensity in the course of the formation of a phagocytic cup (shown in arrow) as performed in
718 *D*.
719 (F) Time-lapse confocal images of wild type and Sptlc2$^{-/-}$ RAW 264.7 cells transfected with PH(PLCδ)-
720 GFP and infected with Zymosan Alexa Flour 594-conjugate at a MOI of 10. (G) Quantification of the
721 PH(PLCδ) fluorescence intensity in the course of the formation of a phagocytic cup (shown in arrow) as
722 performed in *F*.
723 (H) Time-lapse confocal images of wild type and Sptlc2$^{-/-}$ RAW 264.7 cells transfected with PH(AKT)-
724 GFP and infected with Zymosan Alexa Flour 594-conjugate at a MOI of 10. (I) Quantification of the
725 PH(AKT) fluorescence intensity in the course of the formation of a phagocytic cup (shown in arrow) as
726 performed in *H*.
727 Accumulation of GFP signal to site of particle binding was quantified by the ratio of increased GPF signal
728 intensity at the phagosome versus the GFP signal across entire cell at the indicted points. Intensity profiles
729 of 5-10 cells are represented. Data are mean ± SD. *$p<0.05$, **$p<0.01$, two-tailed unpaired t-test, ns = not
730 significant.
731
732
733

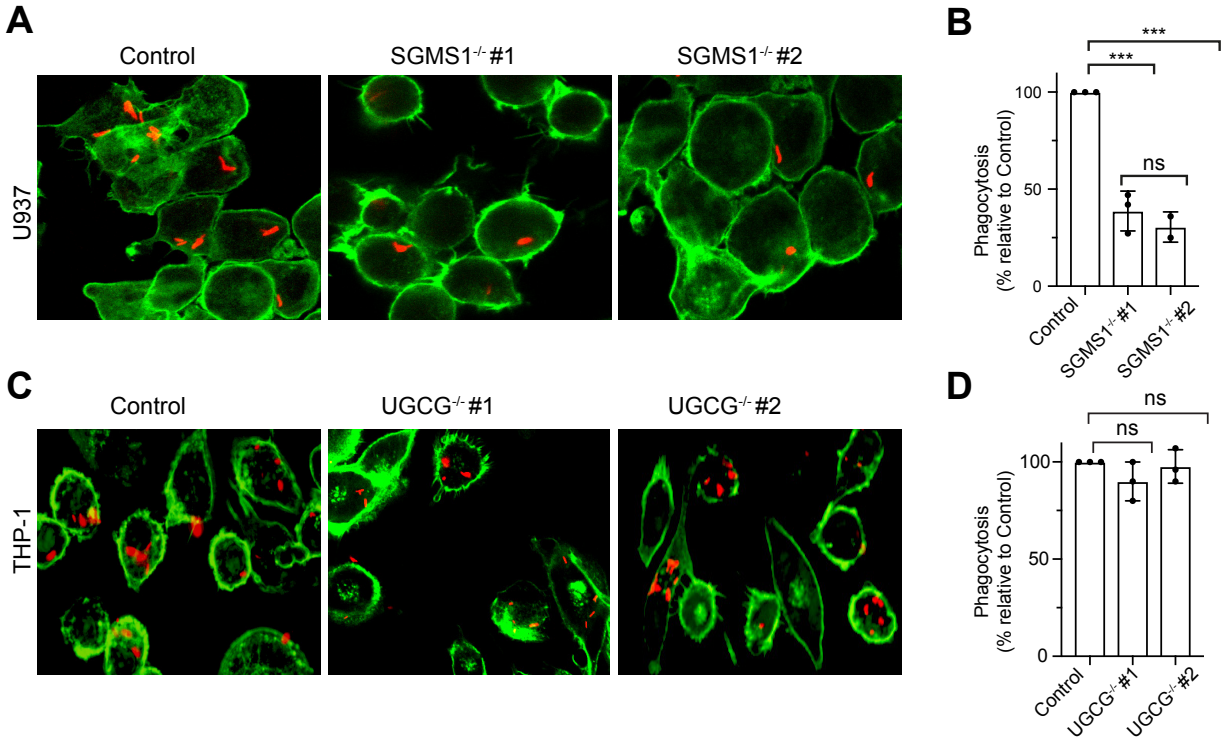

Figure 6: Production of sphingomyelin, not glycosphingolipids, is critical for efficient Mtb uptake
(A) Representative images of U937 wild type and two different SGMS1 knockout cell lines infected with mCherry-expressing Mtb for 2h. (B) Quantification of Mtb uptake for experiments described as in *A*. (C) Representative images of THP-1 wild type and two different UGCG knockout cell lines infected with mCherry-expressing Mtb for 2h. (D) Quantification of Mtb uptake for experiments described as in *C*. U937 and THP-1 cells were activated with 50nM PMA for 24 h before Mtb infection. Three independent experiments were performed each in triplicates with at least 1,000 cells quantified per replicate. Data are mean ± SD. ***$p<0.001$, ns = not significant, two-tailed unpaired t-test.

745 **Movie Legends:**

746 **Movie 1.** A movie showing live confocal microscopy imaging of wild type RAW 264.7 cells
747 transfected with the Rac1/Cdc42 biosensor PAK(PBD)–GFP and infected Zymosan-conjugated
748 with Alexa Flour 594 (shown in red) at a MOI of 10.

749

750 **Movie 2.** A movie showing live confocal microscopy imaging of Sptlc2$^{-/-}$ RAW 264.7 cells
751 transfected with the Rac1/Cdc42 biosensor PAK(PBD)–GFP and infected Zymosan-conjugated
752 with Alexa Flour 594 (shown in red) at a MOI of 10.

753

754 **Movie 3.** A movie showing live confocal microscopy imaging of wild type RAW 264.7 cells
755 transfected with the F-actin biosensor LifeAct-GFP and infected with Zymosan-conjugated with
756 Alexa Flour 594 (shown in red) at a MOI of 10.

757

758 **Movie 4.** A movie showing live confocal microscopy imaging of Sptlc2$^{-/-}$ RAW 264.7 cells
759 transfected with the F-actin biosensor LifeAct-GFP and infected with Zymosan-conjugated with
760 Alexa Flour 594 (shown in red) at a MOI of 10.

761

762 **Movie 5.** A movie showing live confocal microscopy imaging of wild type RAW 264.7 cells
763 transfected with the PIP2 biosensor PH(PLCδ)-GFP and infected with Zymosan-conjugated with
764 Alexa Flour 594 (shown in red) at a MOI of 10.

765

766 **Movie 6.** A movie showing live confocal microscopy imaging of Sptlc2$^{-/-}$ RAW 264.7 cells
767 transfected with the PIP2 biosensor PH(PLCδ)-GFP and infected with Zymosan-conjugated with
768 Alexa Flour 594 (shown in red) at a MOI of 10.
769
770 **Movie 7.** A movie showing live confocal microscopy imaging of wild type RAW 264.7 cells
771 transfected with the PIP3 biosensor PH(AKT)-GFP and infected with Zymosan-conjugated with
772 Alexa Flour 594 (shown in red) at a MOI of 10.
773
774 **Movie 8.** A movie showing live confocal microscopy imaging of Sptlc2$^{-/-}$ RAW 264.7 cells
775 transfected with the PIP2 biosensor PH(AKT)-GFP and infected with Zymosan-conjugated with
776 Alexa Flour 594 (shown in red) at a MOI of 10.
777

778 **Supplementary Results**

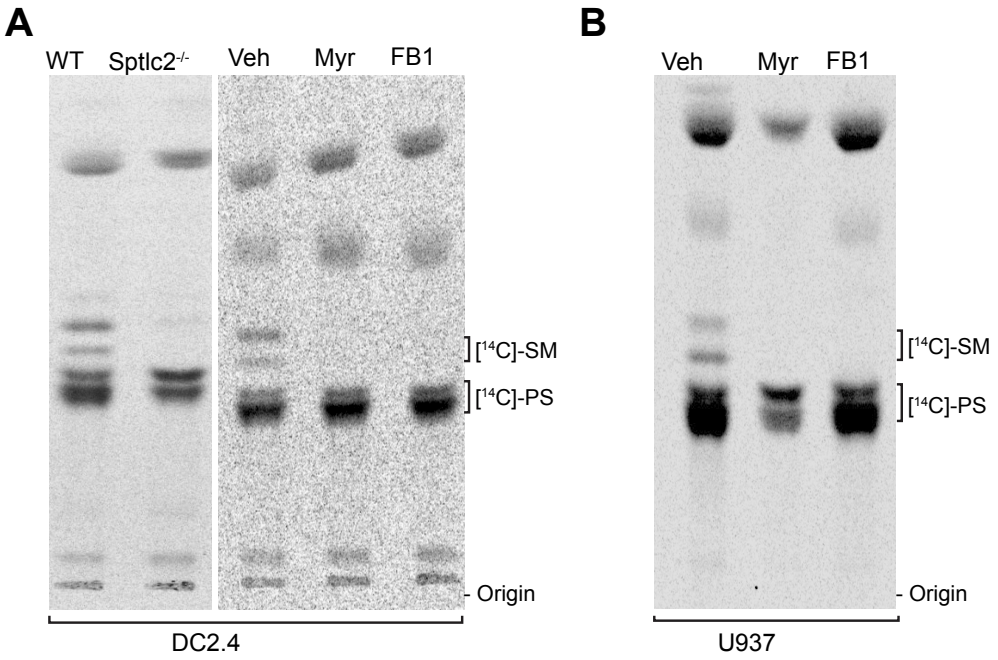

779

780 **Supplemental Figure 1: Genetic and small molecule inhibitors mediated depletion of sphingolipid in**

781 **phagocytes.** (A, B) Control, Sptlc2$^{-/-}$ and inhibitor-treated cells were labeled with the sphingolipid

782 precursor 3-L-[^{14}C]-serine, and total lipids were extracted and analyzed by thin layer chromatography and

783 autoradiography. All data are representative of 3 independent experiments.

784

785

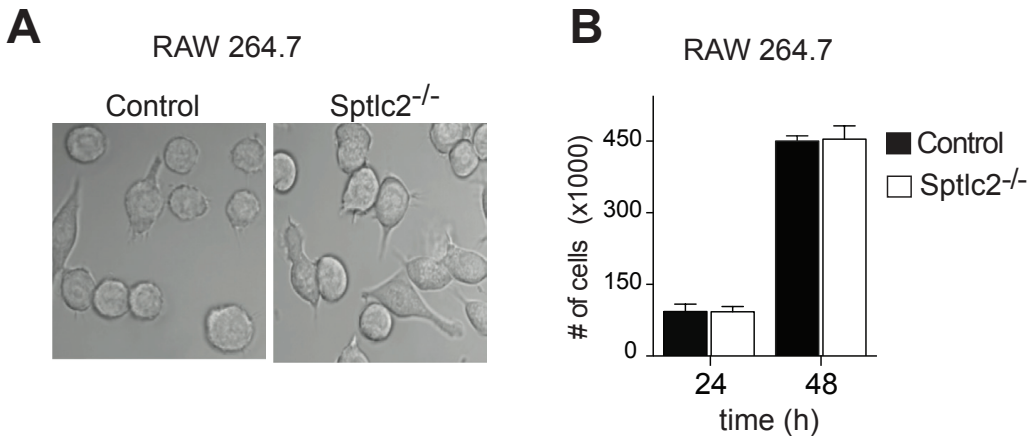

786

787 **Supplemental Figure 2: Depletion of sphingolipids has no significant effect on cell growth.** (A)
788 Microscopy images of control and Sptlc2$^{-/-}$ RAW 264.7 macrophages, showing no morphological difference
789 between the mutant and control cells. (B) The cell division of the control and Sptlc2$^{-/-}$ RAW 264.7
790 macrophages at different time points was measured and presented.
791

792

793

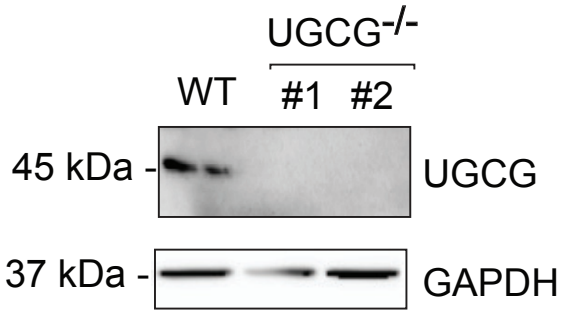

794

795 **Supplemental Figure 3:** Western blot analysis of cell lysates collected from wildtype and two different
796 CRISPR/Cas9 knockout THP-1 cell lines probed using anti-UGCG antibody (upper panel). Antibody
797 against GAPDH was used as a loading control (lower panel).
798